Dalton Transactions

ROYAL SOCIETY OF CHEMISTRY

PAPER

Check for updates

Cite this: DOI: 10.1039/d6dt00379f

Inorganic hybrid materials integrating carbon nanotubes with osmium compounds: formation mechanisms, structure and reactivity

Luke T. Norman,[a] William J. Cull,[a] Craig T. Stoppiello,[a,b] Christopher S. Allen,[c,d] Johannes Biskupek,[e] Maxwell A. Astle,[a] Rhys W. Lodge,[a] Ute Kaiser,[e] Jesum Alves Fernandes,[a] Graham A. Rance *[a,b] and Andrei N. Khlobystov *[a,b]

The formation of inorganic nanomaterials is highly sensitive to the local environment. When environmental conditions are carefully selected, they enable precise control over the composition, shape and dimensionality of inorganic nanostructures, which, in turn, influences their functional properties. In this study, we explore the impact of single-walled carbon nanotubes (SWNTs) on the sequential transformation of triosmium dodecacarbonyl ($Os_3(CO)_{12}$) into osmium iodide (OsI) and subsequently osmium disulphide (OsS_2). Initially, the nanotubes form a van der Waals complex with $Os_3(CO)_{12}$, allowing the molecules to retain their structure and properties, unaffected by the presence of the SWNT, as determined by direct imaging using high-resolution transmission electron microscopy (HRTEM) and evaluation of metal atom valence states by X-ray photoelectron spectroscopy (XPS). When iodine is introduced, it triggers a chemical transformation of the metal carbonyl to iodide (OsI) in a NaCl-like cubic phase. The nanotubes play a crucial role by providing electrons from their valence band, as evidenced by resonance Raman spectroscopy. The structure of OsI depends significantly on its position relative to the nanotube: disk-like particles measuring 4–6 nm form on the exterior, while sub-nanometer-wide wires form within the internal cavity, the latter exhibiting tumbling motion within the SWNT, resulting in different projections in HRTEM images. The hybrid OsI-SWNT material shows ionic character and readily reacts with hydrogen sulphide, converting into OsS_2. During this reaction, SWNTs regain their electrons and become charge neutral. OsS_2 nanoparticles consist of two distinct phases: a standard pyrite-like cubic phase forms the core of the particles, while a hexagonal phase creates the shell (c-OS_2@h-OsS_2). Inside SWNTs, however, OsS_2 forms a nanowire that is one unit cell wide and twists along the length of the nanotube. The nanotube serves as a protective shell for the undercoordinated osmium atoms located at the edges of the nanowire. We showed that in inorganic transformations, the SWNT acts both as a template for the growth of osmium-based nanoparticles and an analytical platform for the detailed characterisation and comparison of nanostructures formed with and without spatial constraints, facilitating the discovery of new crystal phases such as OsI and hybrid nanostructures of c-OS_2@h-OsS_2 reported in this study.

Received 12th February 2026,
Accepted 14th April 2026

DOI: 10.1039/d6dt00379f

rsc.li/dalton

1. Introduction

Control of the dimensions of an inorganic material has been shown to significantly influence its physicochemical properties, often with highly attractive outcomes, including increases in the critical temperature of superconductors, electron mobility in transistor materials, and catalytic activity, *e.g.*, in the hydrogen evolution reaction.[1–3] Single-walled carbon nanotubes (SWNTs), cylinders of graphitic carbon with diameters at the nanoscale (typically between 0.7–2.0 nm) and nearly macroscopic lengths,[4,5] offer a particularly powerful strategy for the controlled growth of nanomaterials, due to the presence of two distinct surfaces – a concave interior and a convex exterior. The convex outer surface promotes the formation of nanomaterials with high, easily accessible, surface areas, suitable for application in catalysis and sensing,[6] whereas the concave inner surface templates the formation of

---

[a] *School of Chemistry, University of Nottingham, Nottingham, NG7 2RD, UK. E-mail: Graham.Rance@nottingham.ac.uk, Andrei.Khlobystov@nottingham.ac.uk*
[b] *Nanoscale and Microscale Research Centre (nmRC), University of Nottingham, Nottingham, NG7 2QL, UK*
[c] *Electron Physical Sciences Imaging Centre, Diamond Light Source Ltd, Oxfordshire, OX11 0DE, UK*
[d] *Department of Materials, University of Oxford, Oxfordshire, OX1 3PH, UK*
[e] *Central Facility of Electron Microscopy, Electron Microscopy Group of Materials Science, University of Ulm, 89081 Ulm, Germany*

quasi-1D materials,[7–10] including unusual nanostructures, such as linear chains of sulphur,[11] selenium[12] or tellurium[13] that do not exist in the bulk, polyhedra of terbium trichloride, $TbCl_3$, with reduced coordination compared to the bulk material,[14] and magnetic nanoribbons based on cobalt phthalocyanine.[15]

The use of SWNTs as templates for nanomaterial growth also enables detailed structural investigation, in direct space and in real time, using transmission electron microscopy (TEM). The transformations of molecular precursors within and on SWNTs can be triggered using stimuli, such as heat[16] or an electron beam,[17] and often lead to products with reduced dimensionality.[10,18] In particular, stepwise reactions that allow the addition of different elements in a desired order and proportion into nanotubes have been demonstrated for metal iodides and metal sulphides, such as MoS_2,[16,19] WS_2,[20] and PtS_2.[21] All these compounds synthesised in the form of nanowires within SWNTs demonstrated only small deviations of bond lengths and angles from the bulk geometry. To harness the divergent environments provided by the concave inner and convex outer surfaces, thereby exploiting the full power of nanoscale confinement in SWNTs, it is necessary to demonstrate control of the atomic structure of a material, as well as its dimensionality, which could be achieved using structurally flexible species that can exist in more than one crystal phase with distinct lattice symmetries. Among the transition metal sulphides, OsS_2 is a good candidate for this purpose as it is currently only known to form a cubic pyrite-type lattice;[22] however, when subjected to confinement within, or adsorption on, SWNTs, there is the possibility that new phases may be discovered. Moreover, the iodides of osmium, in particular the monoiodide (OsI), are considered to be amorphous in bulk,[23] thus SWNTs offer an exciting opportunity for studying complex materials, which do not lend themselves easily to bulk structural analysis, through direct-space imaging of their atomic structures at the nanoscale.

In this work, we demonstrate the synthesis of osmium compounds simultaneously utilising the interior and exterior surfaces of SWNTs, where nanotubes serve as a versatile analytical platform. It is important to note that whilst most related studies explore the independent use of either the internal or external surfaces of SWNTs, we have deliberately used both surfaces simultaneously to enable fair and direct comparison of the impact of confinement on materials grown under identical experimental conditions. Complementary imaging and analysis, using both local-probe (aberration-corrected and high-resolution transmission electron microscopy, AC-HRTEM and HRTEM, respectively, and energy-dispersive X-ray analysis, EDX) and bulk analytical techniques (X-ray photoelectron spectroscopy, XPS and resonance Raman spectroscopy) (Scheme 1), permitted a comprehensive characterisation of the nanomaterials and revealed mechanisms enabling control of the structure, composition and morphology of osmium compounds at the nanoscale, demonstrating the significant impact of the local environment on the growth of inorganic nanostructures.

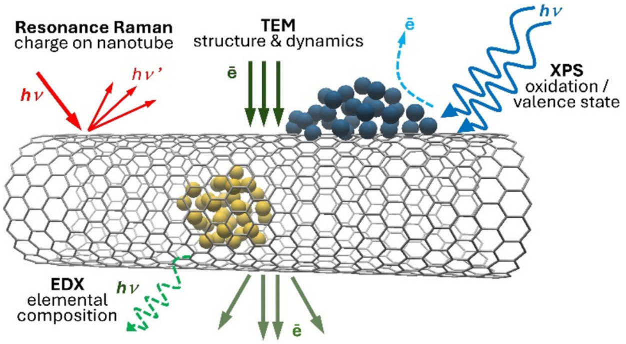

Scheme 1 Carbon nanotubes are an analytical platform that enable complementary imaging and analytical methods to provide comprehensive characterisation of molecular and inorganic nanomaterials. Ensemble-averaging analytical methods probe nanostructures on both the inner and outer surfaces of nanotubes simultaneously, whilst local-probe approaches permit examination at specific locations with nanoscale precision (the lengths of the arrows do not correspond to measured penetration depths).

2. Materials and methods

2.1. Materials

SWNTs (P2-SWNTs, arc-discharge, Carbon Solutions, USA) were annealed at 600 °C for 17 min to remove their end caps and any amorphous carbon, resulting in a 50% mass loss. Triosmium dodecacarbonyl (Alfa Aesar), iodine (Fisher Scientific) and hydrogen sulphide (CK Special Gases) were all used as supplied.

2.1.1. Deposition of triosmium dodecacarbonyl in and on single-walled carbon nanotubes. Freshly opened SWNTs were added to a Pyrex ampoule (d = 10 mm, l = 15 cm) along with triosmium dodecacarbonyl ($Os_3(CO)_{12}$) (10 mg, 0.0055 mmol) and sealed under vacuum (10^{-4} mbar). The ampoule was heated to 130 °C for 3 days and then cooled in an ice bath to cease the sublimation process.

2.1.2. Preparation of osmium iodide in and on SWNTs. Iodine (20 mg, 0.039 mmol) was added to a Pyrex ampoule containing $Os_3(CO)_{12}$/SWNT (5 mg) and sealed under vacuum (10^{-4} mbar). The ampoule was heated for 3 days at 120 °C and then cooled in an ice bath. The resultant material was then heated to 500 °C for 1 hour under argon.

2.1.3. Preparation of osmium disulphide in and on SWNTs. Argon was flowed over the material isolated from the previous step (5 mg) in a tube furnace for 1 hour at room temperature, followed by a flow of hydrogen sulphide at room temperature. The sample was then heated to 550 °C for 2 hours whilst being subjected to a flow of hydrogen sulphide (15 mL min^{-1}). The sample was then cooled under argon at a rate of 5 °C min^{-1} back to room temperature.

2.2. TEM and EDX

Samples were suspended in propan-2-ol and drop-cast onto lacey carbon copper TEM grids (Agar). HRTEM was conducted using a JEOL 2100F FEG-TEM microscope operated at 100 or 200 kV. EDX analysis was performed using an Oxford Instruments INCA X-ray microanalysis system. AC-HRTEM of the osmium iodide nanowires was performed at Ulm University using the C_c/C_s corrected SALVE TEM microscope operated at 60 kV. Acquisition was conducted using a dose rate of 10^6 e^- $(nm^2\ s)^{-1}$ and exposure times of 0.5 to 2 s. AC-HRTEM of the osmium iodide and disulphide nanoparticles was performed at the Electron Physical Science Imaging Centre at Diamond Light Source on a C_s corrected JEM ARM300CF operated at 80 kV.

2.3. TEM simulation

TEM image simulations were carried out using QSTEM, a multi-slice program which uses the Dirac-Fock scattering potential of Rez *et al.*[24] A fixed number of 10 slices per nanotube was chosen, and images were calculated with a sampling of 0.005 nm per pixel. The defocus and aberration parameters were set according to the values used in experimental imaging. The effect of limiting the electron dose on the images was studied using a custom-made Monte Carlo program that applies noise by utilising the Poisson statistics of electrons.

2.4. Resonance Raman spectroscopy

Samples were suspended in methanol and drop-cast onto Si (100) wafers. Resonance Raman spectroscopy was performed on a HORIBA LabRAM HR Raman microscope using either a 532 or 660 nm laser (at ~0.2 mW power), a 100× objective and a 200 μm confocal pinhole. To simultaneously scan a range of Raman shifts, a 600 lines per mm rotatable diffraction grating along a path length of 800 mm was employed, conferring a spectral resolution better than 1.9 and 1.2 cm^{-1} for the 532 and 660 nm lasers, respectively. Spectra were detected using a Synapse CCD detector (1024 pixels) thermoelectrically cooled to −60 °C. Before spectra collection, the instrument was calibrated using the zero-order line and a standard Si (100) reference band at 520.7 cm^{-1}. Spectra were acquired over a minimum range of 125–3400 cm^{-1} with an acquisition time of 15–120 seconds and 2 accumulations to automatically remove the spikes due to cosmic rays and improve the signal-to-noise ratio. Spectra were collected from at least three random locations and averaged to give a mean spectrum.

2.5. Infrared spectroscopy

Infrared spectroscopy was performed on samples in the form of KBr pellets using a Bruker FT-IR spectrometer over the range of 600–4000 cm^{-1}.

2.6. XPS

Samples were analysed using a Kratos AXIS ULTRA with a mono-chromated Al kα X-ray source (1486.6 eV) operated at 10 mA emission current and 12 kV anode potential (120 W). Spectra were acquired with the Kratos VISION II software. A charge neutraliser filament was used to prevent surface charging. Hybrid-slot mode was used, measuring a sample area of approximately 300 × 700 μm. The analysis chamber pressure was better than 5×10^{-9} mbar. Three areas per sample were analysed. A wide scan was performed at low resolution (binding energy range 1400 to −5 eV, with a pass energy of 80 eV, step size of 0.5 eV and a sweep time of 20 minutes). High-resolution spectra at pass energy 20 eV, step of 0.1 eV, and sweep times of 10 minutes each were also acquired for photoelectron peaks from the detected elements, and these were used to model the chemical composition. The spectra were charge-corrected to the C 1s peak at 284.5 eV.

3. Results and discussion

3.1. Interactions of triosmium dodecacarbonyl with carbon nanotubes

Organometallic complexes of osmium, such triosmium dodecacarbonyl, $Os_3(CO)_{12}$, and $[Os_3(CO)_{10}(NCMe)_2]$, have been demonstrated previously as effective precursors for the formation of osmium metal clusters generated in nanotubes[25] and on the surfaces of turbostratic graphite[26] and multi-walled carbon nanotubes (MWNTs).[27] An exohedral fullerene, $[Os_3(CO)_{11}(\eta^2\text{-}C_{60})]$,[28] has also been encapsulated in SWNTs employing strong van der Waals interactions between the fullerene cage and the concave surface of the nanotube to drive encapsulation of the osmium clusters.[29] Osmium complexes have also been used to functionalise the SWNT sidewall by cycloaddition of osmium tetroxide, OsO_4, under photoirradiation, which enabled tuning of the electronic properties of the SWNTs by increasing their resistance.[30] In this study, $Os_3(CO)_{12}$ was selected as the starting point for subsequent chemical transformations because it can be easily converted to other forms of osmium without generating any impurities (*e.g.* residual ligands).[29] In the first step, $Os_3(CO)_{12}$ was combined with SWNTs by sublimation *in vacuo* (Fig. S1), to ensure deposition of $Os_3(CO)_{12}$ on both the interior and exterior surfaces of SWNTs.

HRTEM imaging using 100 kV e-beam and low electron dose conditions (5.1×10^4 e^- nm^{-2}) provided optimum conditions for studying $Os_3(CO)_{12}$ molecules within the nanotubes, appearing as high-contrast elliptical features (Fig. 1a). Previous attempts to image delicate metal carbonyl complexes within SWNTs have been unsuccessful, as the e-beam in TEM is known to rapidly break metal–ligand bonds, leading to "naked" metal clusters, for example, the formation of Re nanoparticles within SWNTs by e-beam irradiation of rhenium carbonyl at accelerating voltages of 80 and 100 kV.[31] However, under our low-dose imaging conditions, discrete molecular species, approximately 0.65 nm in diameter, translating and rotating within the confines of the SWNTs, were observed. The image analysis demonstrates the complementary fit of $Os_3(CO)_{12}$ and the 1.2 nm diameter SWNTs; the guest molecules are large enough to form close van der Waals' contacts with the host-nanotube, but have sufficient space to rotate freely within SWNTs, adopting different orientations observed in the HRTEM images (Fig. 1b inset). EDX analysis confirmed that the features observed in the TEM images contained only carbon, oxygen, and osmium (Fig. 1b); however, meaningful

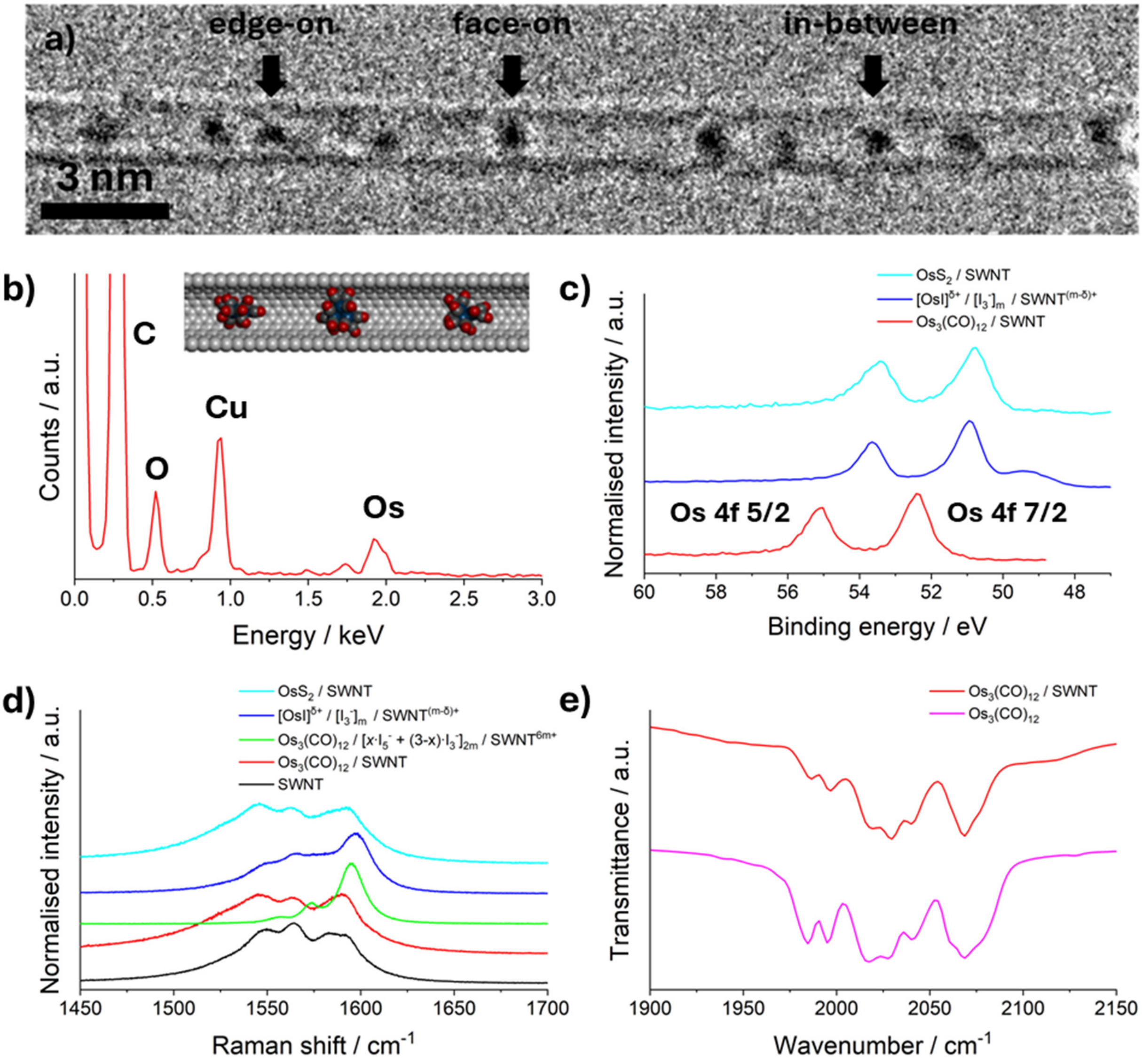

Fig. 1 (a) 100 kV HRTEM image of $Os_3(CO)_{12}$/SWNT material where triosmium dodecacarbonyl molecules are encapsulated within a 1.2 nm diameter SWNT. (b) EDX spectrum of $Os_3(CO)_{12}$/SWNT displaying the presence of carbon, oxygen, and osmium (the copper peak is due to the TEM grid). Inset is a structural model of triosmium dodecacarbonyl molecules within a 1.2 nm SWNT shown in three different orientations – edge-on, face-on and in-between (left to right), matching the examples of $Os_3(CO)_{12}$ projections observed in experimental HRTEM images shown in (a). (c) Comparison of XP spectra in the region of the osmium 4f 5/2 and 7/2 peaks for $Os_3(CO)_{12}$/SWNT (red), $[OsI]^{\delta+}/[I_3^-]_m/SWNT^{(m-\delta)+}$ (blue) and OsS_2/SWNT (light blue). The spectra have been normalised to the Os 4f 7/2 peak intensity. (d) Comparison of the 660 nm resonance Raman spectra showing the G-band of each material during stepwise synthesis: empty SWNTs (black), $Os_3(CO)_{12}$/SWNT (red), $Os_3(CO)_{12}/[x{\cdot}I_5^- + (3-x){\cdot}I_3^-]_{2m}/SWNT^{6m+}$ (green), $[OsI]^{\delta+}/[I_3^-]_m/SWNT^{(m-\delta)+}$ (blue), and OsS_2/SWNT (light blue). The spectra have been normalised to the G-band intensity. (e) The carbonyl region of IR spectra showing free $Os_3(CO)_{12}$ (purple) and $Os_3(CO)_{12}$/SWNT (red). The spectra in (c), (d) and (e) have been offset on the *y*-axis to ease visual comparison.

quantification was not possible owing to the contribution of the nanotube itself to the carbon and oxygen signal intensities. After prolonged exposure (5 min) to the 100 keV electron beam, the carbonyl ligands are cleaved off, and the molecules transform into metallic osmium clusters, which promote the etching of the nanotube sidewall in an electron beam-induced ejection (EBIE) process (Fig. S2).[32] It was not possible to visualise $Os_3(CO)_{12}$ adsorbed on SWNTs by HRTEM due to their high mobility in an unconfined state, and vaporisation in the vacuum of the TEM column; however, their presence was unambiguously determined based on their subsequent reactivity, as described in the following section. In either case, the interactions between $Os_3(CO)_{12}$ and SWNTs appeared to be driven solely by van der Waals forces, as evidenced by no significant shift in the position of the G-band in the 660 nm resonance Raman spectrum of $Os_3(CO)_{12}$/SWNT, relative to empty metallic SWNTs (Fig. 1d and Fig. S3a), indicating little to no charge transfer from $Os_3(CO)_{12}$ to SWNTs. However, subtle shifts in the position of the radial breathing modes (RBMs, $-3.2\ cm^{-1}$), compared to the parent SWNTs, were observed, which are known to occur when depositing molecular species on either of the surfaces of SWNTs (Fig. S3b).[33,34] The presence of carbonyl ligands within $Os_3(CO)_{12}$/SWNT was confirmed by infrared spectroscopy (Fig. 1e), with all carbonyl vibrational modes of $Os_3(CO)_{12}$ (1985, 1995, 2016, 2028, 2042 and 2068 cm^{-1}) observed. The Os 4f 7/2 binding energy was recorded at 52.4 eV in the X-ray photoelectron spectra (XPS) of $Os_3(CO)_{12}$/SWNT (Fig. 1c, Fig. S4a, and Table S1), which is higher than that expected for metallic osmium (50.8 eV) and reported previously for free $Os_3(CO)_{12}$ molecules (51.6 eV),[35] consistent with the known π-acceptor character of the CO ligands. Overall, no measurable electron density redistribution or orbital re-hybridisation in $Os_3(CO)_{12}$/SWNT suggests that it is a simple composite material with interactions between the components mediated by van der Waals forces.

3.2. Reactions of $Os_3(CO)_{12}$/SWNT complex with iodine

The introduction of iodine in the $Os_3(CO)_{12}$/SWNT system (Fig. S1) changed the nature of interactions. Firstly, the G-band of metallic SWNTs, resonantly enhanced under 660 nm excitation, shifted by +3.6 cm^{-1} compared to empty SWNTs (Fig. 1d). Additionally, there was a change in the shape of the G-band to resemble a Lorentzian profile, which is consistent with a metallic to semiconducting transition.[36] These are both indicative of electron transfer from the SWNTs to molecules. The emergence of additional bands at 109 and 175 cm^{-1} in the 532 nm resonance Raman spectra indicates the formation of I_3^- and I_5^- polyiodide anions, respectively.[37] The latter significantly overlaps with one of the RBMs of the SWNT host, but is evidenced by the second, third, and fourth harmonics (Fig. S5).[38] The iodine molecules act as electron acceptors to the nanotube (eqn (1)), followed by a reaction of thus-formed iodide anions with one or two additional I_2 molecules, leading to the formation of polyiodides (eqn (2)), yielding $Os_3(CO)_{12}/[x{\cdot}I_5^- + (3-x){\cdot}I_3^-]_{2m}/SWNT^{6m+}$ hybrid material, where electrostatic interactions between the molecules and nanotubes become dominant.

$$m{\cdot}I_2 + \mathrm{SWNT} \rightarrow 2m{\cdot}\mathrm{I}^- + \mathrm{SWNT}^{2m+} \tag{1}$$

$$6m{\cdot}\mathrm{I}^- + 2m(x+3){\cdot}I_2 \rightarrow 2mx{\cdot}I_5^- + 2m(3-x){\cdot}I_3^-, \quad \text{where } 0 < x < 3 \tag{2}$$

532 nm resonance Raman spectroscopy measurements after heating the material at 500 °C reveals the conversion of I_5^- to I_3^- as indicated by changes in the relative intensities of the polyiodide anion bands (Fig. S5b); however, we note that as both SWNT and I_m^- Raman bands are sensitive to resonance processes, accurate quantification is challenging. Furthermore, the G-band of SWNTs in the 660 nm resonance Raman spectrum is shifted by a further +2 cm^{-1} after the heat treatment, indicating a more electron-withdrawing nature of the compounds formed in and around the nanotubes. The XP binding energy of the osmium 4f 7/2 shifts to 51.0 eV after heating (Fig. 1c and Fig. S4b), which is in the range for metal iodides, including Os(I), with the binding energy of the iodine 3d 5/2 peak (619.3 eV) within the range of metal iodide species (Fig. S4c and Table S1).[39]

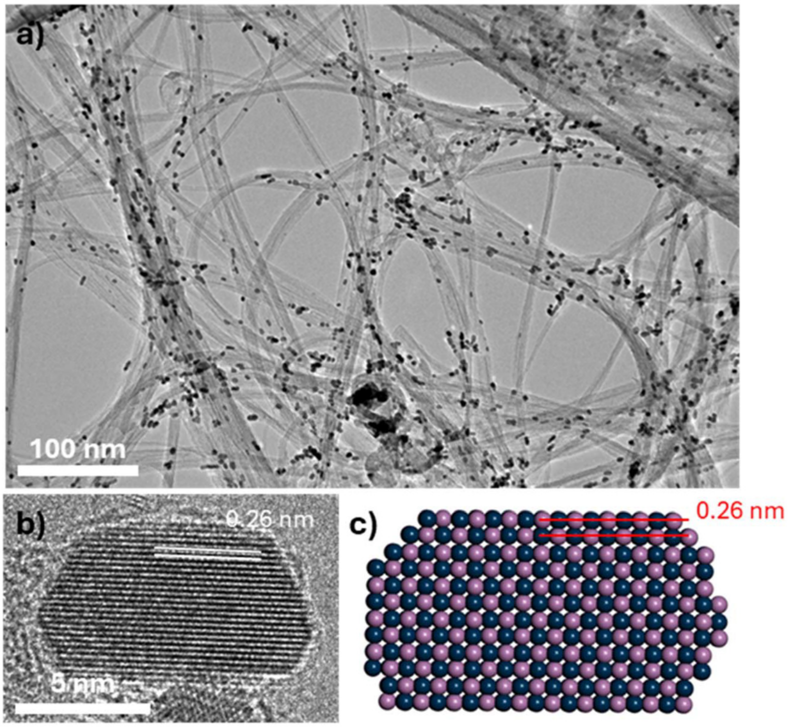

Fig. 2 (a) 200 kV HRTEM large field of view image of $[OsI]^{\delta+}/[I_3^-]_m/SWNT^{(m-\delta)+}$ showing nanoparticles on the exterior of the SWNTs. (b) 80 kV AC-HRTEM image of an OsI nanoparticle showing 0.26 nm *d*-spacing. (c) Structural model of a cubic NaCl-lattice showing 0.26 nm *d*-spacing. The blue and pink spheres represent osmium and iodine atoms, respectively.

TEM imaging of the material after heat treatment revealed the presence of nanoparticles on the exterior of SWNT bundles, which had grown during the thermal activation process (Fig. 2a). Nanoparticle size analysis indicates a size range between 2 and 8 nm with a mean diameter of 5.1 ± 0.9 nm. AC-HRTEM imaging of a nanoparticle supported on the exterior nanotube surface showed it was crystalline with a regular *d*-spacing of 0.26 nm (Fig. 2b). This was also evident in images of two overlapping nanoparticles in projection, which exhibited the same spacing as well as having a second area in which a hexagonal pattern was identified (Fig. S6a). Local EDX analysis of a single nanoparticle shows the presence of osmium and iodine in a 1 : 1.2 stoichiometry and thus the formation of osmium mono-iodide on the convex surface of SWNTs (Fig. S6b). The two projections observed in AC-HRTEM, coupled with EDX quantification, are consistent with a NaCl-type structure, with both osmium and iodine in six-coordinate environments (Fig. 2c). Considering the TEM data in conjunction with the resonance Raman spectroscopy observations above indicates that pentaiodide anions serve as oxidants towards osmium during heat treatment (eqn (3)).

$$2\mathrm{Os}_3(\mathrm{CO})_{12} + 3{\cdot}I_5{}^- \rightarrow 6{\cdot}\mathrm{OsI} + 3{\cdot}I_3{}^- + 24{\cdot}\mathrm{CO} \qquad (3)$$

The thus-formed material, therefore, can be described by the empirical formula $[\mathrm{OsI}]^{\delta+}/[I_3{}^-]_m/\mathrm{SWNT}^{(m-\delta)+}$, bearing in mind that osmium iodide is slightly more electron withdrawing towards the nanotubes, as compared to the osmium dodecacarbonyl, due to the increased oxidation state of the metal centres, which explains a heightened positive charge on the nanotube indicated by the G-band shift in the Raman spectra as discussed above.

AC-HRTEM at 60 kV was used to inspect species formed within the nanotubes upon heating, revealing (Fig. 3a–c and Fig. S7) two-atom thick nanowires within a 1.71 nm SWNT that rotate and translate independently of each other and extend along the full length of the nanotube. The dose rate during imaging was 2.0×10^6 e^- $(\mathrm{nm}^2\ \mathrm{s})^{-1}$. EDX analysis of a bundle of SWNTs filled with nanowires (Fig. 3f) shows a near 1 : 1 ratio of Os : I, signifying the formation of osmium mono-iodide within the nanotubes, as observed for the exterior nanoparticles.[20]

The distance between each OsI nanowire and the nanotube concave surface was measured as 0.31 nm, which corresponds to a typical van der Waals gap in graphitic materials.[40] The rotations, around the nanotube axis, of the nanowires allow detailed analysis of the structure across multiple projections. The contrast of the features along each row of atoms is consistently similar, indicating that this is due to an osmium and an iodine atom overlapping in the image projection.[21] The top nanowire in Fig. 3c has measured distances between nearest neighbours of 0.31 and 0.36 nm. A structural model was proposed, based on the interatomic distances measured and corresponds to a distorted cubic NaCl-type phase with only osmium-iodine bonds present and each iodine bonded to only three osmium atoms (Fig. 3d and e). Structural models of the nanowires in orientations matching the AC-HRTEM images were created, and subsequently generated AC-HRTEM simulations were in good agreement with them (Fig. 3a–e, and Fig. S8). The third image of the time-series shows the two nanowires in different projections with the bottom nanowire appearing as two parallel lines, attributed to a tilt in the nanowire axis (Fig. 3c). The distance between the two lines was found to be 0.28 nm, which is close to the *d*-spacing observed in the exterior nanoparticles (0.26 nm). Whilst the TEM images in Fig. 3b and c show the presence of two nanowires in different orientations, the TEM image in Fig. 3a shows four rows of atoms in proximity. Additionally, the contrast of the middle two rows of atoms is significantly higher than that of the top and bottom rows. These two phenomena arise from the nanowires being in 45° rotations from their face-on view, and one of the nanowires rotating in the SWNT to be in front of the other, overlapping two rows of atoms, causing higher

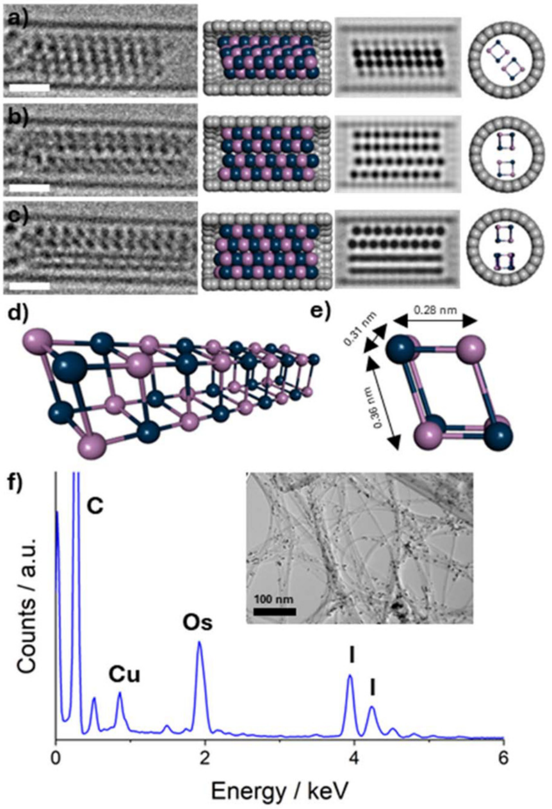

Fig. 3 (a–c) 60 kV AC-HRTEM image of $[\mathrm{OsI}]^{\delta+}/[I_3{}^-]_m/\mathrm{SWNT}^{(m-\delta)+}$ (left) showing two osmium iodide nanowires (a) overlapping in projection, (b) demonstrating the gap between the nanowires and (c) the bottom nanowire rotating perpendicular to the nanotube axis. The scale bar is 1 nm. Structural models showing the proposed orientations of the nanowires inside the SWNT host (middle left) (blue and pink spheres represent osmium and iodine atoms, respectively), TEM simulations of the proposed models (middle right) and cross-sectional views of the nanowires (right). (d) Structural model of the osmium iodide nanowire. (e) Cross-sectional model of (d). (f) EDX spectrum of $[\mathrm{OsI}]^{\delta+}/[I_3{}^-]_m/\mathrm{SWNT}^{(m-\delta)+}$ showing the presence of osmium and iodine in the sample conducted over an area containing both nanoparticles and nanowires of osmium iodide (inset), (the copper peak is due to the TEM grid, oxygen and carbon from the SWNTs and the support film).

contrast in TEM. Bulk osmium monoiodide was previously shown to be amorphous by Fergusson *et al.*[23] and thus this discovery highlights the important role of SWNTs in templating and stabilising low oxidation and low coordination compounds of osmium, particularly as these were not observed in a control reaction in the absence of SWNTs, which yielded only osmium metal nanoparticles (Fig. S9). It is also worth noting that the distorted cubic OsI formed inside nanotubes has the same structure as that formed outside, both being NaCl-type structures. However, the coordination number of the osmium is three in the nanowires compared to six in the nanoparticles due to spatial confinement effects, with the concave surfaces of SWNTs stabilising the large surface area of OsI nanowires and low-coordinate osmium centres, as well as templating 1D growth, whereas OsI formed without confinement on the convex surfaces of SWNTs is six-coordinate, with a smaller fraction of surface atoms which do not require stabilisation.

3.3. Reactions of low-dimensional osmium iodide with hydrogen sulphide in presence of nanotubes

The reaction of $[\mathrm{OsI}]^{\delta+}/[I_3^-]_m/\mathrm{SWNT}^{(m-\delta)+}$ with hydrogen sulphide at 550 °C (Fig. S1) led to significant changes. Upon reaction, the G-band red-shifted to the original position of empty metallic SWNTs in the 660 nm resonance Raman spectrum, indicating that the nanotubes regain electrons and become charge neutral (Fig. 1d), and polyiodide bands disappeared. Moreover, a new band at 496 cm^{-1} emerges, which may correspond to disulphide (S_2^{2-}) (Fig. S5c). The position of the osmium 4f 7/2 peak in the XP spectrum shifted to 50.8 eV, indicating changes in the oxidation/valence state (Fig. 1c, Fig. S4d, and Table S1). TEM imaging of nanoparticles on the surfaces of the SWNTs revealed compositionally-uniform and core–shell type nanoparticles with a range of 1–3 shells (Fig. 4a–c inset). The mean diameter of all nanoparticles was measured to be 5.3 ± 1.4 nm, commensurate with the corresponding osmium iodide particles in the previous step. Local EDX analysis conducted on core–shell nanoparticles identified osmium and sulphur as constituent elements in a 1 : 1.6 atomic ratio (Fig. 4c).

AC-HRTEM imaging of a core–shell nanoparticle identified the 0.23 nm *d*-spacing of the core, matching the (211) plane of pyrite-type cubic OsS_2 (Fig. 5a),[22] with a different structure of the shell. The AC-HRTEM images of the latter resemble edge-on WS_2 nanoribbons[20] in which a series of high contrast fea-

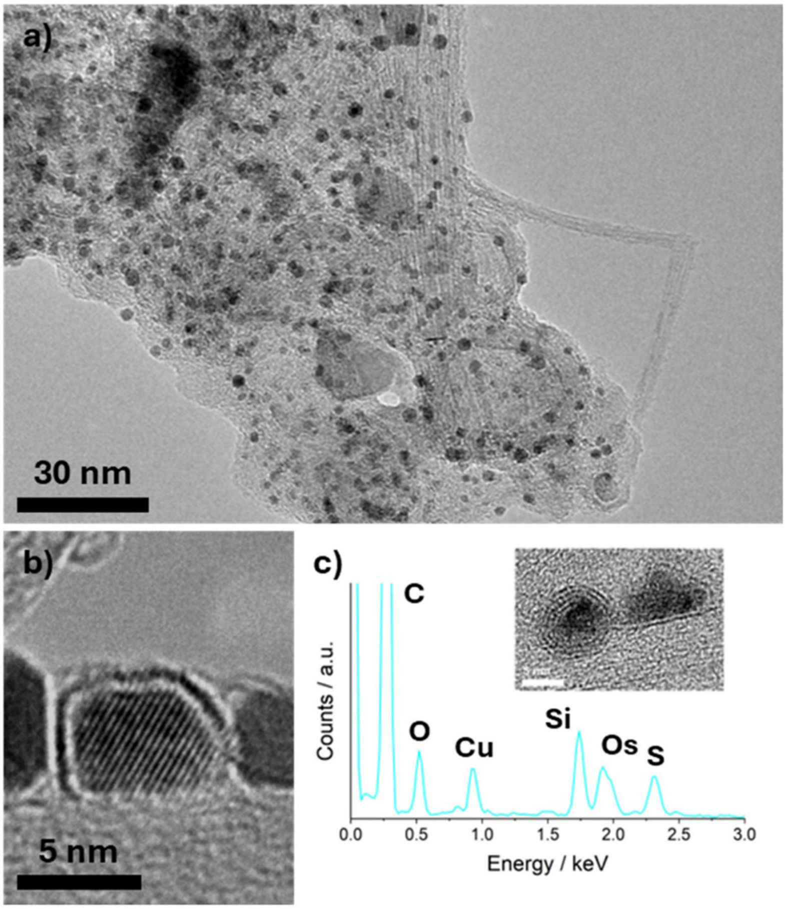

Fig. 4 (a) 200 kV HRTEM image of OsS_2/SWNT highlighting the exterior nanoparticles. (b) 200 kV HRTEM image of osmium disulphide nanoparticles that exhibit core–shell structures. (c) Local EDX spectrum of two core–shell nanoparticles (inset), identifying osmium and sulphur (the copper peak is due to the TEM grid, oxygen and carbon from the SWNTs and the support film, silicon likely from contamination).

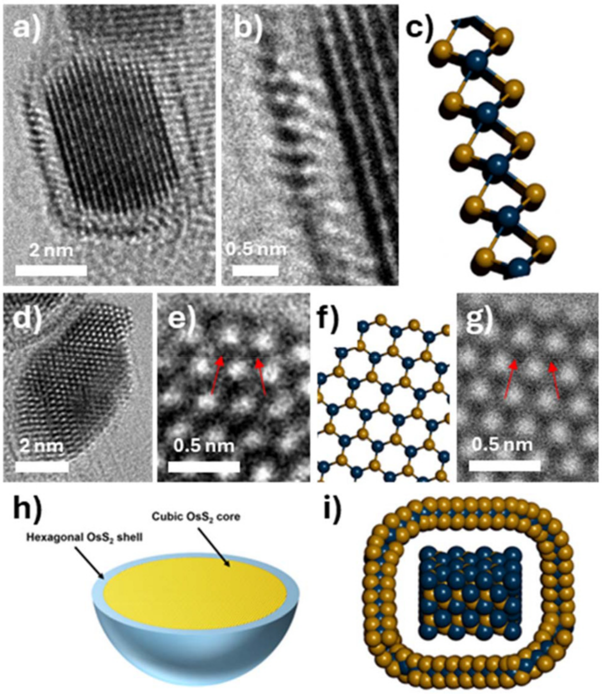

Fig. 5 (a) 80 kV AC-HRTEM image of a core–shell OsS_2 nanoparticle. (b) A digitally magnified image from (a) highlighting the atomic structure of the nanoparticle shell. (c) Structural model of hexagonal OsS_2 in an edge-on view. The blue and yellow spheres represent osmium and sulphur atoms, respectively. (d) 80 kV AC-HRTEM image of a nanoparticle that is partially covered by a shell. (e) A digitally magnified image from (d) highlighting the hexagonal structure of a section of the shell placed over the vacuum. Red arrows are superimposed on the image to indicate the alternating contrast of the lattice. (f) Structural model of hexagonal OsS_2 in a face-on view. (g) HRTEM image simulation based on the structural model in (f), which shows the hexagonal structure. Red arrows are superimposed on the image to indicate the alternating vertex contrast observed in the experimental image. (h) Schematic diagram of the core–shell nanoparticle (yellow – cubic OsS_2, and light blue – hexagonal OsS_2); and (i) a corresponding structural model.

tures, each surrounded by two lower contrast features on either side, correspond to metal and sulphur atoms, respectively. The interatomic distance within the central row of atomic columns was found to be 0.27 nm, suggesting a sheet of hexagonal OsS_2 (isomorphic to hexagonal WS_2) (Fig. 5c). When the cubic OsS_2 core was only partially covered by a shell, a suitable projection showed the hexagonal in-plane structure of the shell (Fig. 5d and e), with alternate contrast intensities of the lattice points and the distance between adjacent high contrast features of 0.24 nm. HRTEM image simulations of a hexagonal OsS_2 layer (Fig. 5f) matched well the experimental images (Fig. 5g), therefore indicating that the core–shell nanoparticles of osmium sulphide are a combination of two different phases of the same material, and can be denoted as c-OsS_2@h-OsS_2, where h and c stand for hexagonal and cubic phases, respectively. The hexagonal metal disulphide phases are commonly observed in molybdenum and tungsten but have not been reported for osmium. Its formation in the core–shell osmium sulphide particles is likely to be dictated by the need to stabilise the dangling bonds of few-nm-sized particles of c-OsS_2, which are not possible to stabilise by the convex surface of SWNT, as the nanotube surface curves away from nanoparticles. The observed situation with c-OsS_2@h-OsS_2 can be viewed as an analogue of core–shell carbon structures, such as nanodiamond@graphene, in which the same chemical element changes its hybridisation in the shell (graphene) to stabilise the highly reactive dangling bonds in the core (nanodiamond).[41,42] However, in the case of core–shell osmium disulphide, it is the oxidation states of the metal and anion that will differ in the core and shell. Considering that h-OsS_2 appears to be isostructural to h-WS_2, it is expected to consist of Os^{4+} and $2S^{2-}$, whilst the pyrite-type c-OsS_2 consists of Os^{2+} and $S_2{}^{2-}$. Therefore, the full transformation of osmium iodide to sulphide can be described as (eqn (4)):

$$\mathrm{OsI} + 2{\cdot}\mathrm{H_2S} + I_3{}^{-} + \mathrm{SWNT}^{+} \rightarrow \mathrm{OsS_2} + 4{\cdot}\mathrm{HI} + \mathrm{SWNT} \tag{4}$$

Followed by the phase transformation on the surface of osmium sulphide particles triggered by temperature (eqn (5)):

$$c\text{-}\mathrm{OsS_2} \rightarrow h\text{-}\mathrm{OsS_2} \tag{5}$$

It is important to note that eqn (4) requires an increase of osmium oxidation state from +1 to +2; this must be balanced by decrease of the positive charge on the nanotubes, with the latter acting as a reversible reservoir of electron density[19] that was donated at the stage of OsI formation and replaced at the stage of OsS_2 formation, such that the nanotubes go back to their charge neutral state, as shown by the shifts of the G-band. Hydrogen iodide evaporates from the material under the reaction conditions (550 °C). The phase transition in reaction 5 may also be accompanied by partial loss of sulphur anions from the surface layer of OsS_2 nanoparticles and by defect formation at the points of bending in the shells, which may be responsible for the lower-than-expected sulphur content observed in EDX. Furthermore, the observed 4f 7/2 Os XP peak is 0.5 eV higher than expected for cubic osmium disulphide with osmium in the +2 state (50.3 eV),[43] indicating that the spectrum is dominated by photoelectrons from the hexagonal shells, where osmium has the formal oxidation state of +4.

The structure of OsS_2 within the SWNT was probed by HRTEM imaging (Fig. 6a), which revealed the formation of a three-atom-thick nanowire measuring 0.6 nm in diameter, corresponding to the unit cell of cubic OsS_2. The encapsulated nanowires exhibit a high degree of translational and rotational motion (Video S1), as previously observed for other metal chalcogenides inside SWNTs.[44] For this reason, real-space imaging with high frame-rate image acquisition (10 frames per second) was utilised in order to obtain snapshots of the encapsulated nanowires in on-axis orientations, which could be compared to simulated HRTEM images for structural evaluation. The nanowire in Fig. 6a extends parallel to the nanotube axis across the entire length of the SWNT (approximately 40 nm in length) and is representative of all filled SWNTs. EDX analysis of a bundle of filled SWNTs confirms the loss of

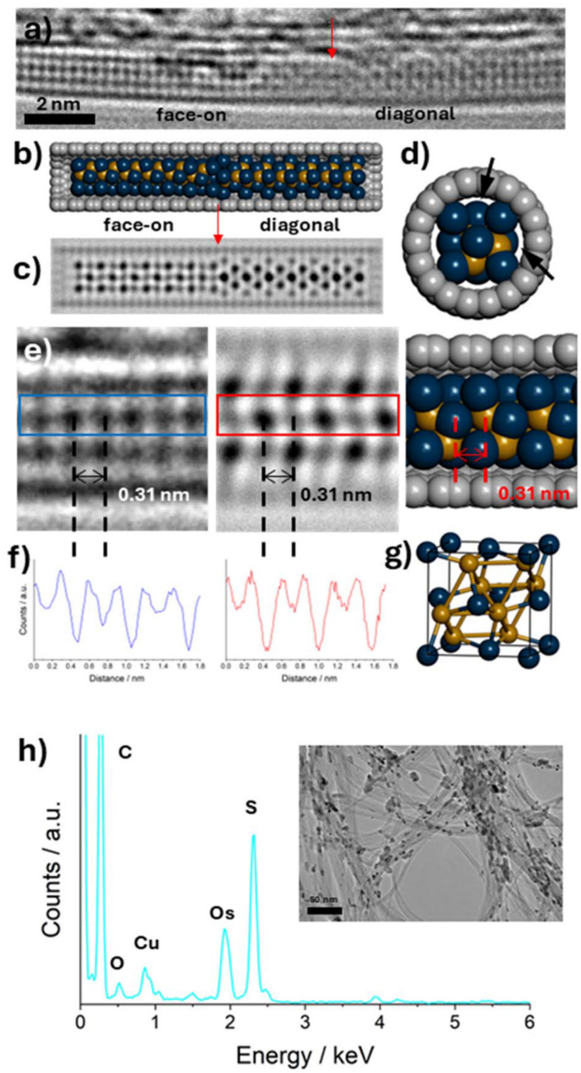

Fig. 6 (a) 100 kV HRTEM image showing a SWNT containing an OsS_2 nanowire. A red arrow indicates the twist point of the nanowire. (b) Structural model showing the 1D *c*-OsS_2 nanowire fit inside the SWNT (blue spheres represent osmium atoms and yellow spheres represent sulphur atoms). (c) HRTEM image simulation of the twisted *c*-OsS_2 nanowire model, highlighting the projections observed in (a). A red arrow indicates the twist point of the nanowire. (d) Structural model showing the cross-section of the host–guest system (the space created by the concave surface of SWNT and a face of the OsS_2 cubic cell, indicated with black arrows, can accommodate additional sulphur atoms). (e) Magnified HRTEM image in (a) showing the periodic distance (0.31 nm) between adjacent atoms (left), HRTEM image simulation demonstrating this periodic distance (middle), based on a structural model (right). (f) Image contrast analysis of the areas shown in the HRTEM image and simulation in (e) evidencing the alternate contrast pattern between adjacent atoms. (g) Unit cell of cubic osmium disulphide. (h) EDX spectrum of an area containing both core–shell nanoparticles and twisted nanowires (inset), identifying both sulphur and osmium present (the copper peak is due to the TEM grid, oxygen and carbon from the SWNTs and the support film).

iodine and the presence of osmium and sulphur in the nanotube (approximate 1 : 3 atomic ratio; Fig. 6h). Image analysis along the rows of atoms, parallel to the nanotube axis, identifies alternating contrast intensities, suggesting that either the OsS_2 nanowire consists of alternate osmium and sulphur atoms, or that there is a difference in the number of atoms overlapping in projection (Fig. 6e and f). Sulphur, compared to osmium, has a far lower atomic number, and thus individual atoms would be difficult to distinguish in HRTEM images.[21] This means that the features observed must correspond to columns containing a varying number of osmium atoms. A face-on projection of the cubic osmium disulphide unit cell has two overlapping osmium atoms on each corner of the unit cell, one osmium atom in the middle of each edge and two overlapping osmium atoms in the centre of the square face (Fig. 6g). HRTEM image simulations based on a model of the nanowire built by extending the unit cell along only one axis, confirmed the alternating contrast pattern observed experimentally as well as the regular spacings observed between columns (0.31 nm) (Fig. 6b and c), consistent with pyrite-type cubic osmium disulphide, but restricted to one-dimensional growth. A closer inspection of the nanowire reveals helical twists, which may maximise the interactions with the nanotube concave surface and relieve strain in the structure. Multiple projections of the nanowire are observed in the TEM image, including face-on and diagonal, and simulations of a twist in the structure are consistent with the proposed structural model (Fig. 6b and c). The cubic phase of OsS_2, extended into a single unit cell wide nanowire, contains a very high proportion of undercoordinated osmium atoms, with those in the edges of the nanowire effectively stabilised by interactions with the SWNT concave surface, which curves around the nanowire, thus negating the need for the shell formation by phase transition to hexagonal OsS_2 as shown for nanoparticles outside of nanotubes (Fig. 5). However, the host nanotube cannot effectively coordinate the osmium atoms in the faces of the cubic nanowire, and the interstitial space formed between the concave side of SWNT and face of OsS_2 cubic cell can accommodate one or two extra atoms of sulphur (indicated with black arrows, Fig. 6d), in a sulphide or disulphide form, respectively, which may explain a higher percentage of sulphur observed by EDX for *c*-OsS_2 nanowires in nanotubes (Fig. 6h).

4. Conclusions

Carbon nanotubes are excellent supports and nanocontainers for inorganic materials and are used in many applications. In this study, we utilised both the external (convex) and internal (concave) surfaces of SWNTs simultaneously and demonstrated the profound impact of surface type on the structure of inorganic nanomaterials, using the transformations of osmium compounds as an example system. Confinement inside nanotubes serves three principal purposes: (i) the nanotube cavity templates the growth of OsI and OsS_2 nanowires along one crystallographic direction, limiting other two dimensions, and (ii) the SWNT concave surface simultaneously wraps around the nanowires of cubic/distorted cubic phases of the osmium compounds thus stabilising highly unstable surfaces of nanowires with a large proportion of dangling bonds/undercoordinated metal atoms, as well as (iii) balancing the charge of the encapsulated species. When the synthesis of osmium compounds occurs on the external convex surface of the nanotube, the absence of spatial confinement allows unrestricted growth in all three dimensions, resulting in plate-like cubic and spheroidal core–shell nanoparticles of OsI and OsS_2, respectively. Atoms in the externally formed OsI are six-coordinate which is drastically reduced to three-coordinate for the distorted cubic OsI inside nanotubes and compensated by interactions between the nanowire and nanotube concave surface conversely, external OsS_2 has the same cubic structure as OsS_2 inside nanotubes, but in order to stabilise its surface atoms, a new form of OsS_2 with a hexagonal lattice, isostructural with WS_2, wraps around the nanoparticle, imitating the nanotube concave surface. The use of nanotubes as platforms for inorganic reactions in this study enabled us to broaden the chemistry of osmium, discover three previously unknown compounds at the nanoscale, and elucidate mechanisms of inorganic nanostructure formation and stabilisation using a holistic analytical approach.

Author contributions

Luke T. Norman: formal analysis, investigation, writing – original draft. William J. Cull: investigation, writing – original draft, writing – review and editing. Craig T. Stoppiello: investigation, writing – original draft. Christopher S. Allen: investigation, writing – original draft. Johannes Biskupek: investigation, writing – original draft. Maxwell A. Astle: investigation, writing – original draft. Rhys W. Lodge: investigation, writing – original draft. Ute Kaiser: investigation, writing – original draft. Jesum Alves Fernandes: investigation, writing – original draft. Graham A. Rance: investigation, writing – original draft, writing – review and editing, supervision. Andrei N. Khlobystov: conceptualisation, writing – original draft, writing – review and editing, supervision, funding acquisition.

Conflicts of interest

There are no conflicts to declare.

Data availability

The data supporting this article have been included as part of the supplementary information (SI). Supplementary information, including additional TEM and structural models, and EDX, resonance Raman and XP spectra, is available. See DOI: https://doi.org/10.1039/d6dt00379f.

Acknowledgements

This work was supported by the Engineering and Physical Sciences Research Council (EPSRC) (grant numbers EP/R024790/1, EP/V000055/1). L. T. N. acknowledges the support of the EPSRC and the University of Nottingham for funding, and the Nanoscale & Microscale Research Centre (nmRC) for access to the instrumentation. W. J. C. acknowledges funding from the Leverhulme Trust (grant number RPG-2022-300). J. B. and U. K. are grateful for the financial support of the German Research Foundation (DFG) (grant number 424798828). We thank Diamond Light Source for access and support in the use of the electron Physical Science Imaging Centre (ePSIC), Instrument E02 (proposal number MG25251-8), which contributed to the results presented here.

References

1 E. Navarro-Moratalla, J. O. Island, S. Manas-Valero, E. Pinilla-Cienfuegos, A. Castellanos-Gomez, J. Quereda, G. Rubio-Bollinger, L. Chirolli, J. A. Silva-Guillen, N. Agrait, G. A. Steele, F. Guinea, H. S. J. van der Zant and E. Coronado, *Nat. Commun.*, 2016, **7**, 1–7.

2 B. Radisavljevic, A. Radenovic, J. Brivio, V. Giacometti and A. Kis, *Nat. Nanotechnol.*, 2011, **6**, 147–150.

3 J. D. Benck, T. R. Hellstern, J. Kibsgaard, P. Chakthranont and T. F. Jaramillo, *ACS Catal.*, 2014, **4**, 3957–3971.

4 S. Iijima and T. Ichihashi, *Nature*, 1993, **363**, 603–605.

5 D. S. Bethune, C. H. Kiang, M. S. de Vries, G. Gorman, R. Savoy, J. Vazquez and R. Beyers, *Nature*, 1993, **363**, 605–607.

6 S. Ju, J. M. Lee, Y. Jung, E. Lee, W. Lee and S.-J. Kim, *Sens. Actuators, B*, 2010, **146**, 122–128.

7 A. A. Eliseev, M. V. Chernysheva, N. I. Verbitskii, E. A. Kiseleva, A. V. Lukashin, Y. D. Tretyakov, N. A. Kiselev, O. M. Zhigalina, R. M. Zakalyukin, A. L. Vasiliev, A. V. Krestinin, J. L. Hutchison and B. Freitag, *Chem. Mater.*, 2009, **21**, 5001–5003.

8 C. E. Giusca, V. Stolojan, J. Sloan, F. Bornert, H. Shiozawa, K. Sader, M. H. Rummeli, B. Buchner and S. R. P. Silva, *Nano Lett.*, 2013, **13**, 4020–4027.

9 M. Nagata, S. Shukla, Y. Nakanishi, Z. Liu, Y.-C. Lin, T. Shiga, Y. Nakamura, T. Koyama, H. Kishida, T. Inoue, N. Kanda, S. Ohno, Y. Sakagawa, K. Suenaga and H. Shinohara, *Nano Lett.*, 2019, **19**, 4845–4851.

10 S. A. Miners, G. A. Rance and A. N. Khlobystov, *Chem. Soc. Rev.*, 2016, **45**, 4727–4746.

11 A. A. Tonkikh, D. V. Rybkovskiy, A. N. Enyashin, E. A. Obraztsova, N. Van Chuc and E. D. Obraztsova, *Carbon*, 2025, **232**, 119806.

12 W. J. Cull, Q. M. Ramasse, J. Biskupek, G. A. Rance, I. Cardillo-Zallo, B. L. Weare, M. W. Fay, R. R. Whitney, L. R. Scammell, J. Alves Fernandes, U. Kaiser, A. Patane and A. N. Khlobystov, *Adv. Mater.*, 2025, **37**, 2501821.

13 P. V. C. Medeiros, S. Marks, J. M. Wynn, A. Vasylenko, Q. M. Ramasse, D. Quigley, J. Sloan and A. J. Morris, *ACS Nano*, 2017, **11**, 6178–6185.

14 C. Xu, J. Sloan, G. Brown, S. Bailey, V. C. Williams, S. Friedrichs, K. S. Coleman, E. Flahaut, J. L. Hutchison,

R. E. Dunin-Borkowski and M. L. H. Green, *Chem. Commun.*, 2000, 2427–2428.

15 A. A. Tonkikh, D. V. Rybkovskiy, E. D. Obraztsova and J. Phys, *Chem. C*, 2023, **127**, 3005–3012.

16 Z. Wang, H. Li, Z. Liu, Z. Shi, J. Lu, K. Suenaga, S.-K. Joung, T. Okazaki, Z. Gu, J. Zhou, Z. Gao, G. Li, S. Sanvito, E. Wang and S. Iijima, *J. Am. Chem. Soc.*, 2010, **132**, 13840–13847.

17 T. W. Chamberlain, J. Biskupek, G. A. Rance, A. Chuvilin, T. J. Alexander, E. Bichoutskaia, U. Kaiser and A. N. Khlobystov, *ACS Nano*, 2012, **6**, 3943–3953.

18 S. A. Miners, G. A. Rance and A. N. Khlobystov, *Chem. Commun.*, 2013, **49**, 5586–5588.

19 A. Botos, J. Biskupek, T. W. Chamberlain, G. A. Rance, C. T. Stoppiello, J. Sloan, Z. Liu, K. Suenaga, U. Kaiser and A. N. Khlobystov, *J. Am. Chem. Soc.*, 2016, **138**, 8175–8183.

20 Z. Wang, K. Zhao, H. Li, Z. Liu, Z. Shi, J. Lu, K. Suenaga, S.-K. Joung, T. Okazaki, Z. Jin, Z. Gu, Z. Gao and S. Iijima, *J. Mater. Chem.*, 2011, **21**, 171–180.

21 C. T. Stoppiello, J. Biskupek, Z. Y. Li, G. A. Rance, A. Botos, R. M. Fogarty, R. A. Bourne, J. Yuan, K. R. J. Lovelock, P. Thompson, M. W. Fay, U. Kaiser, T. W. Chamberlain and A. N. Khlobystov, *Nanoscale*, 2017, **9**, 14385–14394.

22 T. Stingl, B. Muller and H. D. Lutz, *Z. Kristallogr. – Cryst. Mater.*, 1992, **202**, 161.

23 J. E. Fergusson, B. H. Robinson and W. R. Roper, *J. Chem. Soc.*, 1962, 2113–2115.

24 D. Rez, P. Rez and I. Grant, *Acta Crystallogr., Sect. A:Found. Crystallogr.*, 1994, **50**, 481–497.

25 K. Cao, T. Zoberbier, J. Biskupek, A. Botos, R. L. McSweeney, A. Kurtoglu, C. T. Stoppiello, A. V. Markevich, E. Besley, T. W. Chamberlain, U. Kaiser and A. N. Khlobystov, *Nat. Commun.*, 2018, **9**, 3382.

26 A. Pitto-Barry, L. M. A. Perdigao, M. Walker, J. Lawrence, G. Costantini, P. J. Sadler and N. P. E. Barry, *Dalton Trans.*, 2015, **44**, 20308–20311.

27 K.-F. Yung and W.-T. Wong, *J. Cluster Sci.*, 2007, **18**, 51–65.

28 T. W. Chamberlain, N. R. Champness, M. Schroder and A. N. Khlobystov, *Chem. – Eur. J.*, 2011, **17**, 668–674.

29 T. Zoberbier, T. W. Chamberlain, J. Biskupek, N. Kuganathan, S. Eyhusen, E. Bichoutskaia, U. Kaiser and A. N. Khlobystov, *J. Am. Chem. Soc.*, 2012, **134**, 3073–3079.

30 J. Cui, M. Burghard and K. Kern, *Nano Lett.*, 2003, **3**, 613–615.

31 T. W. Chamberlain, T. Zoberbier, J. Biskupek, A. Botos, U. Kaiser and A. N. Khlobystov, *Chem. Sci.*, 2012, **3**, 1919–1924.

32 T. Zoberbier, T. W. Chamberlain, J. Biskupek, M. Suyetin, A. G. Majouga, E. Besley, U. Kaiser and A. N. Khlobystov, *Small*, 2016, **12**, 1649–1657.

33 M. S. Dresselhaus, G. Dresselhaus, R. Saito and A. Jorio, *Phys. Rep.*, 2005, **409**, 47–99.

34 M. V. Kharlamova, C. Kramberger and T. Pichler, *Phys. Status Solidi B*, 2016, **253**, 2433–2439.

35 R. Zanoni, V. Carinci, R. H. Abu-Samn, R. Psaro and C. Dossi, *J. Mol. Struct.*, 1985, **131**, 363–369.

36 M. V. Kharlamova, *Appl. Phys. A*, 2016, **122**, 791.

37 D. M. Krichevsky, L. Shi, V. S. Baturin, D. V. Rybkovsky, Y. Wu, P. V. Fedotov, E. D. Obraztsova, P. O. Kapralov, P. Shilina, K. Fung, C. T. Stoppiello, V. I. Belotelov, A. Khlobystov and A. I. Chernov, *Nanoscale*, 2022, **14**, 1978–1989.

38 L. Grigorian, K. A. Williams, S. Fang, G. U. Sumanasekera, A. L. Loper, E. C. Dickey, S. J. Pennycook and P. C. Eklund, *Phys. Rev. Lett.*, 1998, **80**, 5560–5563.

39 J. F. Moulder, W. F. Stickle, P. E. Sobol and K. D. Bomben, *Handbook of X-ray Photoelectron Spectroscopy: A Reference Book of Standard Spectra for Identification and Interpretation of XPS Data*, Physical Electronics Division, Perkin-Elmer Corporation, 1992.

40 A. N. Khlobystov, D. A. Britz and G. A. D. Briggs, *Acc. Chem. Res.*, 2005, **38**, 901–909.

41 G. Lan, Y. Qiu, J. Fan, X. Wang, H. Tang, W. Han, H. Liu, H. Liu, S. Song and Y. Li, *Chem. Commun.*, 2019, **55**, 1430–1433.

42 B. Liang, L. Zhang, W. Wang, G. Xu, W. Zhang, Y. Zhang, R. Zhang, L. Yang and L. Zhang, *Mater. Res. Express*, 2019, **6**, 045609.

43 T. Schwarzlose, S. Fiechter and W. Jaegermann, *Ber. Bunsenges. Phys. Chem.*, 1992, **96**, 887–893.

44 W. J. Cull, S. T. Skowron, R. Hayter, C. T. Stoppiello, G. A. Rance, J. Biskupek, Z. R. Kudrynskyi, C. S. Allen, T. J. A. Slater, U. Kaiser, A. Patane and A. N. Khlobystov, *ACS Nano*, 2023, **17**, 6062–6072.